

# Field of Interest Prediction for Computer-Aided Mitotic Count

Marc Aubreville      Christof A. Bertram      Christian Marzahl  
Corinne Gurtner      Martina Dettwiler      Anja Schmidt  
Florian Bartenschlager      Sophie Merz      Marco Fragoso  
Olivia Kershaw      Robert Klopffleisch      Andreas Maier

December 15, 2024

## Abstract

**Purpose:** Manual counts of mitotic figures, which are determined in the tumor region with the highest mitotic activity, are a key parameter of most tumor grading schemes. It is however strongly dependent on the area selection. To reduce potential variability of prognosis due to this, we propose to use computer-aided field of interest prediction to assess the area of highest mitotic activity in a whole-slide image.

**Methods:** We evaluated two state-of-the-art methods, all based on the use of deep convolutional neural networks on their ability to predict the mitotic count in digital histopathology slides. We evaluated them on a novel dataset of 32 completely annotated whole slide images from canine cutaneous mast cell tumors (CMCT) and one publicly available human mamma carcinoma (HMC) dataset. We first compared the mitotic counts (MC) predicted by the two models with the ground truth MC on both data sets. Second, for the CMCT data set, we compared the computationally predicted position and MC of the area of highest mitotic activity with size-equivalent areas selected by eight veterinary pathologists.

**Results:** We found a high correlation between the mitotic count as predicted by the models (Pearson's correlation coefficient between 0.931 and 0.962 for the CMCT data set and between 0.801 and 0.986 for the HMC data set) on the slides. For the CMCT data set, this is also reflected in the predicted position representing mitotic counts in mostly the upper quartile of the slide's ground truth MC distribution. Further, we found strong differences between experts in position selection.

**Conclusion:** While the mitotic counts in areas selected by the experts substantially varied, both algorithmic approaches were consistently able to generate a good estimate of the area of highest mitotic count. To achieve better inter-rater agreement, we propose to use computer-based area selection for manual mitotic count.

# 1 Introduction

Patients with tumors profit significantly from a targeted treatment, and a key to this is the assessment of prognostic factors [35]. Cells undergoing cell division (mitotic figures) are an important factor in this: It is widely accepted that the relative density of cells in mitosis state, the so-called mitotic activity, strongly correlates with cell proliferation, which is amongst the most powerful predictors for biological tumor behavior [4, 10, 21]. Consequentially, mitotic activity is a key parameter in the majority of tumor grading systems for the assessment of hematoxylin and eosin stained histology images and provides meaningful information for treatment considerations in clinical practice [6, 11, 16].

The scheme by Elston and Ellis which is commonly used to assess human breast cancer proposes the count of mitotic figures within ten standardized areas at  $400\times$  magnification (high power field, HPF) resulting in the mitotic count. Prognosis is determined by the mitotic count being between  $0 - 9$ ,  $10 - 19$  and  $> 20$  for a low, moderate and high score with respect to malignancy of the tumor [11]. The grading system by Kiupel *et al.* for the assessment of canine cutaneous mast cell tumors requires at least 7 mitotic figures per 10 HPF for the classification as high grade, i.e. more malignant, tumor [16].

Common to most grading schemes is the recommendation to count mitotic figures in the area with the highest mitotic density, commonly assumed to be in a highly cellular area in the periphery of the tumor section [3, 23, 24, 35]. As has been long assumed by many experts, we have recently confirmed for the case of canine cutaneous mast cell tumors that mitotic figures can have a patchy distribution throughout the tumor section (unpublished data). Naturally, the selection of the area will be influenced by a subjective component and is additionally restricted by limited time in a diagnostic setting.

The count of mitotic figures is known to have low reproducibility [5, 25, 26, 7]. While a low inter-rater agreement of mitotic figures will be one reason for some variance in mitotic count between experts [25], the area selected for counting has certainly a significant influence, as shown by Lozanski *et al.* [19].

As Bonert and Tate pointed out, the mere sampling problem underlying mitosis count caused by the sparse distribution is calling for an increase of the number of high power fields to be counted within [8], an observation also underlined by Meyer *et al.*[26]. Manual count of mitotic figures is, however, a tedious and labor-intensive process, which puts a natural restriction to this number in a clinical diagnostic setting. With increasing number of HPF the mitotic count will converge towards the average MC of the slide, which contradicts the idea of assessment in the most malignant area of the tumor, where the result is likely to have the greatest prognostic value.

For an improved reproducibility and accuracy of the manual mitotic figure count, we thus assume that an automatic preselection of the tumor area with the highest mitotic activity is a crucial step. As shown previously, this selection process can be well performed by the use of deep learning methodologies [2]. In this work, we compared two different approaches, all derived from or inspired by state-of-the-art convolutional neural networks (CNNs), and assessed their ability to estimate the area of highest mitotic activity on the slide. On a data set of completely annotated whole slide images

(WSI), we compared their performance against the selection of five board-certified veterinary pathologists and three veterinary pathologists in training.

## 2 Related Work

Mitotic figure detection is a known task in computer vision for more than three decades, starting with early approaches by Kaman *et al.* using low resolution grayscale images. It took until the advent of deep learning technologies, first used by Cireřan *et al.* [9], for acceptable results to be achieved. The models used in this approach are commonly pixel classifiers trained with images where a mitotic figure is either at the center (positive sample) or not (negative sample). In recent years, significant advances were made in this field, fostered also by several competitions held on this topic [33, 35, 36]. Especially the introduction of deeper residual networks [13] and object detection methods like Faster-RCNN[31] had a large influence on current methods, e.g. the DeepMitosis framework by Li *et al.* [17].

Even though results as achieved by Li *et al.* on the 2012 ICPR MITOS data set[33] with F1-scores of up to 0.831 are impressive, they will likely still not meet clinical requirements, and also might have acceptance problems with experts, since robustness to factors like staining differences and image quality have not yet been proven. Additionally, the data sets overestimate the prevalence of mitotic figures, as large parts of the tumor were excluded from annotation and partially high power fields without any mitotic figure were excluded [36].

Lozanski *et al.* have shown that inter-rater concordance of grades for count of centroblasts significantly benefits from a preselection of HPF [19]. Fauzi *et al.* have shown that computer-aided preselection systems for HPF can increase overall reader accuracy [12] in follicular lymphoma grading based on density of centroblasts. We thus propose to predict the area of highest mitotic activity in a complete WSI to aid the human expert in finding a more accurate prognosis.

## 3 Material

We evaluated the methods on two data sets that represent the current largest data sets in their respective category. The first and much larger data set is from whole slide images (WSI) of canine cutaneous mast cell tumors (a common hematopoietic tumor in dogs), whereas the second consists of slide cut-outs showing human breast cancer (a common epithelial tumor in women).

### 3.1 Canine cutaneous mast cell tumor (CMCT) dataset

Our research group built a data set consisting of 32 canine cutaneous mast cell tumors, where all mitotic figures have been annotated within the entire tumor area of each slide. All tissue samples were taken from routine diagnostic service, i.e. no animal was harmed for the construction of the data set. Tumors were formalin-fixed, cut along the largest diameter and paraffin-embedded. The slides were stained with standard

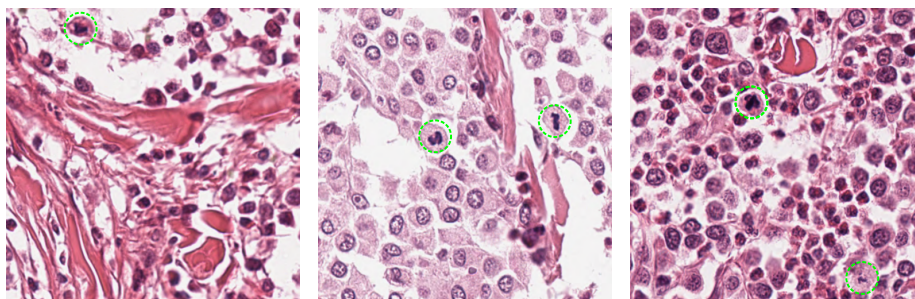


Figure 1: Example images of size 512x512 px (approx. 128x128 $\mu m$ ) from the canine cutaneous mast cell tumor data set. Mitotic figures are marked as green dashed circles.

hematoxylin and eosin dyes using a tissue stainer (ST5010 Autostainer XL, Leica, Germany), prior to being digitized using a linear scanner (Aperio ScanScope CS2, Leica Biosystems, Germany) at a magnification of 400 $\times$  (resolution: 0.25  $\frac{\mu m}{px}$ ).

Using a novel open source software solution [1], it was possible to build up a database that includes annotations for both true mitotic figures and look-alikes that might prove hard to differentiate. This was performed blinded by two experts. For this, the software provides an aided screening mode where the expert is guided over all areas of the WSI where tissue is present. The second expert was unable to see the classification made by the first expert, but saw the location of annotations and provided a secondary opinion for previously annotated cells. In a follow up step, both experts were presented with cells on which no agreement was reached and found a common consensus. This procedure enabled generation of a high quality mitotic figure data set that is unprecedented in size to date, leading to a total count of 42,652 mitotic figures and 70,551 non-mitotic cells that could be mistaken for mitotic cells. The total tumor area in all 32 cases is 4,939 $mm^2$  ( $\mu = 149.68mm^2, \sigma = 96.99mm^2$ ).

This novel data set provides us, for the first time, with the possibility to assess at a large scale the performance of algorithms for region of interest detection, or also more broadly for mitosis detection on complete WSI in general. Using this data set, we can derive a (position-dependent) ground truth MC by counting all mitotic figures in a window of 10 HPF size around the given position, and thus evaluate how the MC depends on the position used for counting. To perform cross-validation, we split up the slide set into three batches of ten slides each, i.e. the training set always consisted of 22 slides for each fold.

An analysis of this data set underlines the assumption that the distribution of mitotic figures is not uniform but rather patchy (see Fig. 2), which further highlights the need of proper selection of the high power fields for reproducible manual count.

### 3.2 Human mamma carcinoma (HMC) dataset

As a second data set, we used the largest currently publicly available mitosis data set, which was released as part of the Tumor Proliferation Assessment Challenge 2016 (TUPAC16) [36]. The data set consists of 23 cases originally published as part of

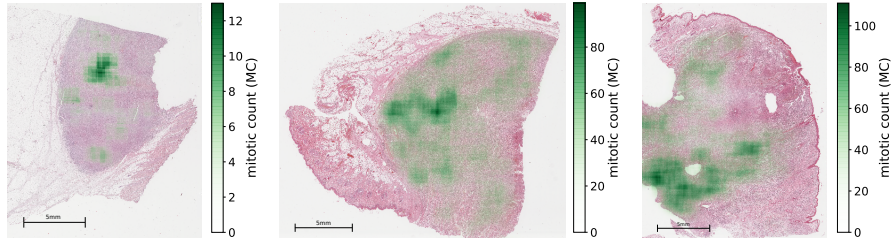


Figure 2: Mitotic count (count of mitotic figures per 10 HPF area), represented as green overlay, from the canine cutaneous mast cell tumor data set.

Part	Case numbers	Number of files	Area	Number of mitotic figures
1	1 to 14	336	$84.0mm^2$	569
2	15 to 31	278	$83.5mm^2$	538
3	32 to 73	42	$84.0mm^2$	445

Table 1: Split of the TUPAC16 data set for our experiments. Case numbers 24 and above have images with  $2mm^2$  size, while 23 and below have  $0.25mm^2$  image size.

the AMIDA13 challenge [35] with varying numbers (10 to 67) of image patches of  $0.25mm^2$  area, and another 50 cases of  $2mm^2$  area. In total, the data set covers 73 cases with a total area of  $251.5mm^2$  and a total count of mitotic figures of 1,552.

As described by Veta *et al.*, the area for annotation was selected by a single expert for each slide. [36] Further, high power fields including not at least one mitotic figure were partially excluded from the data set, unless the total number of HPFs would go below ten [35]. Since the annotation covers only a small part of the overall tumor, it can not be used to test the algorithms aimed at finding the area with highest mitotic activity. However, it is well suited for a comparison of overall correlation between mitotic count estimators and ground truth.

Since the annotation data of the test set is not publicly available, we performed the following split on the published data: We divided the available set into three parts of approximately equal area (see Table 1), where one part will serve as test set and the remainder will be used as training sets. The parts will take over different roles during cross-validation.

## 4 Methods

In this work our aim was to compare field of interest detection for algorithmic approaches versus the current gold standard, i.e. the manual selection by a trained and experienced pathologist. The main focus lay in the evaluation of the CMCT data set, as it provides complete annotations and extensive possibilities for evaluation.

## 4.1 Human Performance Evaluation

In order to set a baseline for the task, we asked five board-certified veterinary pathologists (BCVP) and three veterinary pathologists in training (VPIT) to mark the region of interest spanning 10 HPF they would select in order to evaluate the mitotic count, as required by the grading scheme. The experts came from three different institutions. For this, we set no time limit, but we instructed them to act as they would for normal diagnostics. The pathologists evaluated all 32 slides of our data set. For veterinary pathology, Meuten *et al.* proposed to use  $2.37\text{ mm}^2$  as standard size for ten HPF [24]. The area aspect ratio is the same as being used for the algorithmic pipeline (4:3).

## 4.2 General Algorithmic Approach

We compared two state-of-the-art methods, both aiming at the prediction of the mitotic count within a defined area of a histology slide. The first followed the indirect approach of predicting a mitotic figure map based on supervised classification, while the second tried to directly estimate the number of mitotic figures within an image. For both methods, the original WSI was split up into a multitude of single images that were subsequently processed using a neural network. The result was concatenated to yield a scaled estimate for the mitotic density (see Fig. 3). All approaches were embedded into a toolchain where the estimator is followed by a concatenation and a 2D moving average (MA) operation. The filter kernel of this operation is in accordance with the width and height of the field of interest, i.e. the size of ten HPF. After the MA operator, the position of the maximum value within a valid mask  $V$  is determined as center of the region of interest.

The valid mask generation pipeline (lower branch of Fig. 3) performs a thresholding operation [28] on a downsized version of the WSI, followed by morphological closing. This gives a good estimate of slide area filled by tissue. In order to exclude field of interest predictions in border areas of the slide that are not to at least 95 % covered by tissue, we perform a MA operator of same dimensionality followed by a threshold of 0.95, yielding the valid mask  $V$  (see Fig. 3).

All experiments were carried out on a Linux workstation with NVIDIA GeForce GTX 1080 graphics card.

## 4.3 Estimation of mitotic count using maps (AlgoMap)

While mitotic figure detection is usually considered an object detection task, where the position, class and presence probability of an object are estimated, we wanted to estimate a map of mitosis likelihoods for a given image. While, for the object detection case, a minimum distance between possible mitotic figures needs to be defined for the non-maximum-suppression scheme, this is not needed when deriving a segmentation map.

One approach that has been successfully used in a significant number of segmentation tasks is the U-Net by Ronneberger *et al.* [32]. As previously shown, this approach can be utilized well for the given task [2]. The target map for the network consists of filled circles, wherever a mitotic figure was present. We assume that this shape is a

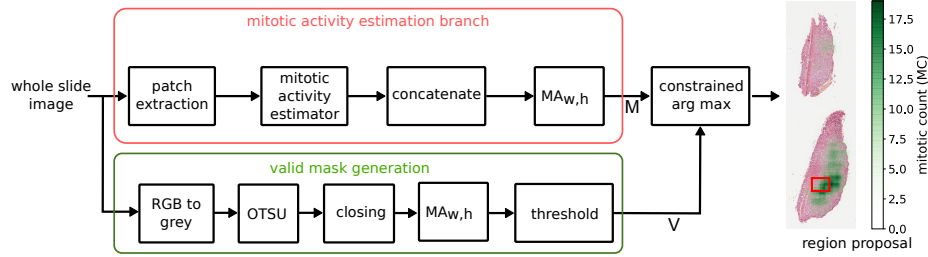


Figure 3: Overview of the general framework. The CNN-based mitotic density estimator is applied on each WSI image patch. After the calculation, a moving window averaging operation yields mitotic density over the area of 10 high power fields. Adapted from [2]

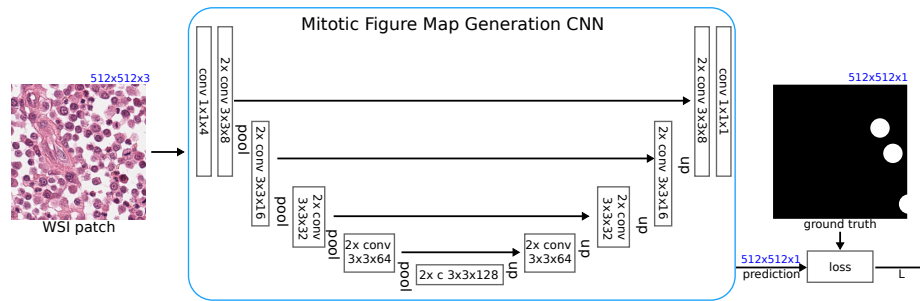


Figure 4: Mitotic figure map generation (AlgoMap) based on Ronneberger's U-Net architecture[32], as described in [2].

good estimate to represent the wide range of possible appearances a mitotic figure can have.

#### 4.3.1 Training and Model Selection

Besides the train-test split mentioned, we divided the training WSI into a training portion (upper 80% of the WSI) and a validation portion (remainder). For training, the batches consisted of randomly sampled RGB images that were by probability of one third:

1. Images containing at least one mitotic figure.
2. Images containing at least one non-mitotic figure (hard negative example), as annotated by pathology experts.
3. Images randomly picked on a slide, i.e. inclusion of mitotic figures is possible but not likely.

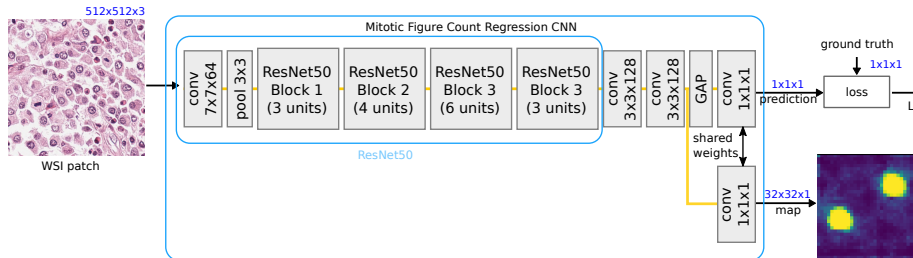


Figure 5: Regression of mitotic count per image (AlgoReg). The lower path is utilized as weakly-supervised path to attain insights into the network’s decision process.

Each group of images had a dedicated justification of inclusion: While it is certainly beneficial to include images with at least one mitotic figure for the network to converge, the inclusion of hard negatives is well known in literature, although commonly in the form of hard example mining from the data set [36]. Finally, we include random picks to also train the network on tissue where no mitotic figure can be expected. This is especially interesting for necrotic tissue, where nuclei can have mitosis-like appearance and for border regions of the slide.

All images were randomly sampled from the training WSI using the criteria described above and were additionally rotated arbitrarily prior to cropping. Since WSI are typically very large (in the order of several Gigapixels), this resulted in a vast number of combinations. For validation, after 10,000 iterations a completely random pick of 5,000 images was fed to the network. The training batch severely overestimates the a priori probability of a mitotic figure being present, but we found that this setup speeds up model convergence significantly. After around 1,500,000 single iterations, the models had typically converged, as observable by the validation loss.

Even though the choice of images alleviates the heavily skewed distribution, the loss function still needs to be chosen appropriately to cater with imbalanced sets. For this reason, we used negative intersection over union as loss[30]

$$L_{IoU} = - \frac{\sum_{\rho \in P} (X_{\rho} + Y_{\rho})}{\sum_{\rho \in P} (X_{\rho} + Y_{\rho} - X_{\rho} Y_{\rho})} \quad (1)$$

where  $X$  and  $Y$  are model output and ground truth map, respectively, and  $\rho$  and  $P$  are a pixel position and the totality of all pixels in a validation image, respectively. We trained the model using the ADAM adaptation method [14] in TensorFlow with an initial learning rate of  $10^{-3}$ . For model selection, we used the model state which yielded the highest F1-score during validation.



#### 4.4 Regression of the mitotic figure count within an image patch (AlgoReg)

Direct estimation of the mitotic figure count is the most straight-forward way of deriving the area with highest mitotic activity in the slide. We use a convolutional neural network with a single output value to regress the (normalized) mitotic count for each inference run.

As also performed by other authors in the field [17, 29], we based the network architecture of this approach on the very successful ResNet50 layout [13]. This network architecture provides deep structures aimed at mapping complex input output relations, and circumvents the vanishing gradient problem by using identity layers. Each subsequent layer only models a residual change to the preceding layer and gradients can be back-propagated easier to the first layers of the network. To the ResNet50 stem, we attached a new head consisting of a double layer of  $3 \times 3$  convolutions (with 128 filter depth each) and batch normalization, followed by a global average pooling layer (GAP) and a final  $1 \times 1$  convolutional layer with filter depth of 1 and sigmoid activation (see Fig. 5).

This architecture is closely related to the one presented by Oquab *et al.*[27] and refined by Zhou *et al.*[37], in that it only has one final  $1 \times 1$  2D convolution layer after the GAP layer. As shown by Oquab *et al.*, this network layout can also serve for object localization in a weakly-supervised approach. For this, the same final convolutional layer (i.e. with equal weights) is attached before the GAP operation. Since all regions of the original feature map have the same contribution to the final output value, the resulting class activation map (CAM) can be interpreted for object localization. It also gives us insights into what portion of the image the network considers discriminative for locating a mitotic figure.

To define the count of mitotic figures in an image, including partial mitotic figures in the border regions of the image (with width  $w$  and height  $h$ ), we denote the  $x$  and  $y$  position of each mitotic figure in coordinates relative to the image center as  $p_x$  and  $p_y$ , respectively. The approximated diameter of a mitotic figure is denoted  $d$ . The overall count, i.e. the target for the regression, is then defined as:

$$C = \frac{1}{\beta} \sum_i \frac{\gamma(|p_x(i)| - \frac{w}{2})\gamma(|p_y(i)| - \frac{h}{2})}{d^2} \quad (2)$$

where the partial weight  $\gamma(x)$  in dependency of the positional offset is defined as:

$$\gamma(x) = \begin{cases} d & x < \frac{d}{2} \\ \frac{d}{2} - x & 0 \leq x < d \\ 0 & x > \frac{d}{2} \end{cases} \quad (3)$$

This approximates border region (i.e. only partially shown) mitotic figures with a square shape. The normalization parameter  $\beta$  was chosen heuristically as  $\beta = 10$ , as this yields a sensible absolute maximum for the total mitotic count in an image patch. As loss function, we use the quadratic error ( $L^2$ ) for each image.

Method Cross-val	CMCT			HMC		
	fold 1	fold 2	fold 3	fold 1	fold 2	fold 3
Mitosis map (AlgoMap)	0.931	0.955	0.956	0.986	0.856	0.833
MC regression (AlgoReg)	0.957	0.942	0.962	0.894	0.957	0.801

Table 2: Pearson correlation coefficient between ground truth mitotic count and estimated mitotic count on all evaluated models, data sets and all folds of the cross-validation.

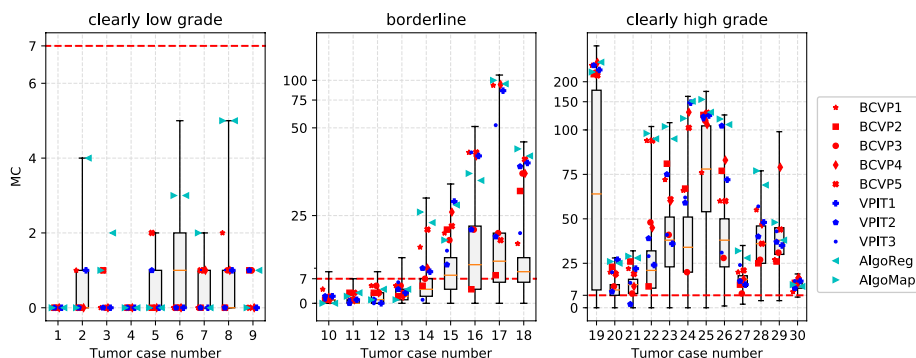


Figure 6: Results of field of interest selection on CMCT data set, as expressed by the resulting ground truth mitotic count (MC) by five board-certified veterinary pathologists (BCVP), three veterinary pathologists in training (VPIT) and the two algorithmic approaches (AlgoReg, AlgoMap). Box-whisker plots indicate the distribution of MC in the tumor area. Figure shows merged results of three-fold cross-validation, ordered by probability of exceeding the high grade threshold by arbitrary field of interest choice. Red dotted line shows threshold as per Kiupel’s grading scheme.

## 5 Results

Our method aims at finding the field of interest with the highest mitotic count. For the HMC data set, data is only available for a subpart of the slide. We were thus only able to evaluate the correlation between the ground truth number of mitotic figures per case and the estimated number. For the CMCT data set, we were able to compare the MC (as per ground truth annotations) at the predicted position with the general distribution of MC for different positions.

### 5.1 Estimation of Mitotic Count

Dependent on the size of the field of view, the number of mitotic figures varies. For the CMCT data set, we always compared for an area of 10 HPF, as per Kiupel’s scheme. For the HMC (TUPAC16) data set, we calculated the correlation coefficient between the sum of all detections and the ground truth number of mitotic objects per case, as no information about geometric positioning of the single images within the original slide

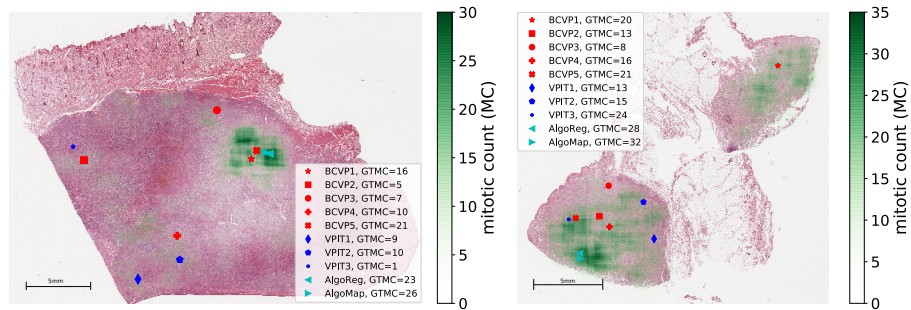


Figure 7: Tumor cases 14 (left) and 27 (right) with color coded mitotic count overlay and results as per ground truth mitotic count of experts and algorithms. Markings indicate the center of the selected area of interest. Clearly, the different choice of area by the expert lead to large differences in the count of mitotic figures (ground truth mitotic count, GTMC) in that area.

was given by the authors of the data set.

### 5.1.1 HMC data set

For the HMC data set, we found generally convincing correlations (between 0.801 and 0.986), but with a significant variance depending on fold and method (see Table 2). It should be noted, however, that these results were achieved on a rather small numerical base, with case numbers between 14 and 42 (see Table 1), which could cause the high variance.

### 5.1.2 CMCT data set

For the CMCT data set, we found a high correlation (correlation coefficients are between 0.931 and 0.962) between the ground truth MC and the predicted MC for both approaches presented in this paper, as shown in Table 2. Per whole slide image of the test set, the average calculation time was 7 minutes, 53 seconds (min=02:16, max=13:19) for AlgoReg or 8 minutes and 3 seconds (min=02:17, max=13:44) for AlgoMap.

## 5.2 Field of interest prediction on CMCT data set

Depending on the first quartile of the MC distribution, we split up the joint results of all cross-validation folds into three groups (see Fig.6): Tumor cases 1 - 9 have not a single possible field of size 10 HPF that contains more than 7 mitotic figures and are thus clearly low grade. Cases 10-18 show a strong dependency of the MC on the area selected and can thus be considered borderline cases, while cases 19-30 reach the threshold value of 7 for 75% of all selections and are thus clearly high grade.

As stated, we included expert area selections for comparison in this work. We found strong differences between the positions the experts chose, and also in the ground truth

mitotic count represented by the respective position (see Fig. 6 and 7). We found no clear difference in performance between the group of board-certified veterinary pathologists and pathologists in training.

For both algorithmic approaches, we found results predominantly above the upper quartile of the MC distribution. For the group of mostly low grade tumors (left plot in Fig. 6), the regression approach was on average the better estimator for the area of highest mitotic activity. However, in this group not a single case with a possible MC of greater than 7 was present, so the choice of region plays a subordinate role. For the group of borderline cases (center plot in Fig. 6), the choice of area is of much greater importance, as it would likely impact the grading result. Here, cases 10-13 most likely would be scored as low grade as per Kiupel’s grading scheme. For cases 14, 17 and 18 (case 14 shown in left panel of Fig.7), both algorithmic approaches outperformed all the human experts. Generally, the regression approach (AlgoReg) showed more stable results in this regard, being better than at least 3 human experts for the borderline cases. With the exception of case 15, however, the map-based approach (AlgoMap) performed slightly better. In the group of high grade tumors (cases 19-30), both algorithmic approaches were able to perform better or on par with all human experts in the majority of cases (20 to 23 and 25 to 28). As also observable in the correlation to the ground truth MC, both methods had a similar performance and varied slightly across slides.

### 5.3 Mitosis Activation Maps

As described in section 4.4, the direct regression approach can be also used for weakly-supervised mitosis detection. The secondary output port of Fig. 5 can be interpreted as model attention leading the the regression output value on the primary output port. We observed that the models generated round activation patterns around mitotic figures in this setup (see Fig. 5). In order to evaluate the size of these on both data sets, we calculated the area where the class activation map exceeded the threshold of 0.5 for images where exactly one mitotic figure was present (as per ground truth annotations)

As depicted in Fig. 8, the area used by the model to count a mitotic figure as such was rather similar for all validation folds, being around  $700-900\mu m$ . For the HMC dataset, we found a greater variation, but also higher median values for the different folds. This result could point to the slight difference in size in both data sets.

## 6 Discussion

Our results support the hypothesis that one significant reason of high rater disagreement in mitotic count, which is well described in literature for human as well as for veterinary pathology, lies in the selection of high power fields used for counting. On our data set, we found the distribution of mitoses to be rather patchy, and selection of area does thus have a strong impact on mitotic count. This emphasizes the importance of this preselection task, which was not tackled in any mitosis detection challenge up to now.

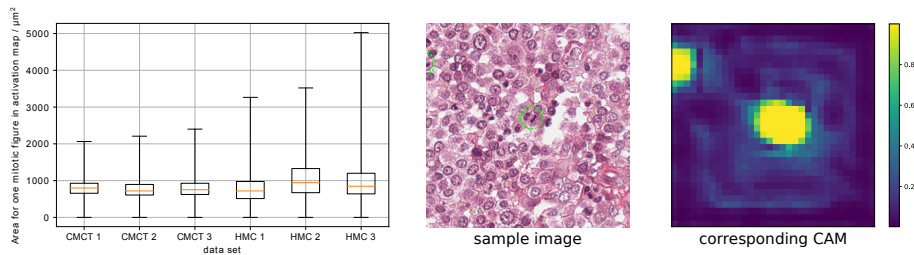


Figure 8: Left: Area investigation for class activation maps in canine cutaneous mast cell tumor (CMCT) and human mamma carcinoma (HMC) data set. Middle: Sample image with annotated mitotic figures (green circles). Right: Corresponding class activation map.

Our work also underlines that while human experts will likely not be consistently able to select the area of highest mitotic activity, an algorithmic evaluation of the WSI could prove to be a good augmentation method. Besides finding the area of highest mitotic activity, the methods presented in this paper can also well serve as an aid to navigate the whole slide image and could thus generate further insights for a more precise diagnosis.

A limitation of current grading ambitions is the poor consistency of the applied grading methods between the different systems. Whereas most grading systems require a mitotic count in ten consecutive, non-overlapping HPF in the area with the highest mitotic density [3, 11, 16, 20, 34] other systems count mitotic figures in three fields [15] or propose random selection of individual HPF [15, 18]. To the authors' best knowledge, current literature does not imply which method has the best agreement with prognosis. In the present work, we have therefore decided to use the criteria of the respective grading system, i.e. ten consecutive HPF in the area within the highest density and a size of the HPF in consensus with current guidelines [24]. A potential limitation is that we had to preset the aspect ratio of the field of interest. We assume that while the actual shape of this area might play a role for an individual case, on average the impact will be negligible. The effect of this, however, will have to be investigated further for data sets where prognostic data is available.

Reproducibility is a key component to each diagnostic method, as also pointed out by Meuten [22]. A clear definition of the criteria and methods used for counting, which is essential in this regard, should thus try to reduce individual factors as much as possible. As such, also a manual pseudo-random selection of areas should be questioned due to non-existent reproducibility. While the computer-aided methods will have limitations and not be error-proof, they can increase inter-rater concordance on average if they deliver better performance than the average human expert. Therefore we propose that the present algorithm with absolute reproducibility has the potential to improve diagnostic prognostication as well as grading system development.

The non-existence of large-scale data sets of completely annotated whole slide tumor sections in many biomedical domains poses an important problem to algorithmic

as well as computer-aided diagnosis in this regard. Our study shows that there is a huge potential for novel methods once such data sets exist also for other species and tissues.

Current grading schemes were mostly developed in retrospect [6, 16, 22], with consideration of the survival rates of the patients and the manual mitotic count. Since the slides were not investigated for mitotic figures within the complete tumor area, the mitotically most active region was necessarily unknown and was possibly missed. Considering our findings, it is possible that those grading schemes have been based on false low MCs. Novel methods like those presented in this paper can thus help to develop more precise and reproducible grading schemes, which will then likely have adjusted thresholds.

## Compliance with ethical standards

All procedures performed in studies involving animals were in accordance with the ethical standards of the institution or practice at which the studies were conducted. The authors declare no conflicts of interest.

## References

- [1] Aubreville, M., Bertram, C.A., Klopffleisch, R., Maier, A.: SlideRunner - A Tool for Massive Cell Annotations in Whole Slide Images. In: A. Maier, T.M. Deserno, H. Handels, K.H. Maier-Hein, C. Palm, T. Tolxdorff (eds.) *Bildverarbeitung für die Medizin 2018 - Algorithmen - Systeme - Anwendungen. Proceedings des Workshops vom 11. bis 13. März 2018 in Erlangen*, pp. 309–314. Springer Vieweg, Berlin, Heidelberg (2018)
- [2] Aubreville, M., Bertram, C.A., Klopffleisch, R., Maier, A.: Augmented Mitotic Cell Count using Field Of Interest Proposal. In: *Bildverarbeitung für die Medizin* (accepted) (2019)
- [3] Azzola, M.F., Shaw, H.M., Thompson, J.F., Soong, S.j., Scolyer, R.A., Watson, G.F., Colman, M.H., Zhang, Y.: Tumor mitotic rate is a more powerful prognostic indicator than ulceration in patients with primary cutaneous melanoma. *Cancer* **97**(6), 1488–1498 (2003)
- [4] Baak, J.P.A., Gudlaugsson, E., Skaland, I., Guo, L.H.R., Klos, J., Lende, T.H., Søyland, H., Janssen, E.A.M., zur Hausen, A.: Proliferation is the strongest prognosticator in node-negative breast cancer: significance, error sources, alternatives and comparison with molecular prognostic markers. *Breast Cancer Research and Treatment* **115**(2), 241–254 (2008)
- [5] Bertram, C.A., Gurtner, C., Dettwiler, M., Kershaw, O., Dietert, K., Pieper, L., Pischon, H., Gruber, A.D., Klopffleisch, R.: Validation of Digital Microscopy Compared With Light Microscopy for the Diagnosis of Canine Cutaneous Tumors. *Veterinary Pathology* **55**(4), 490–500 (2018)

- [6] Bloom, H.J.G., Richardson, W.W.: Histological Grading and Prognosis in Breast Cancer. *British Journal of Cancer* **11**(3), 359–377 (1957)
- [7] Boiesen, P., Bendahl, P.O., Anagnostaki, L., Domanski, H., Holm, E., Idvall, I., Johansson, S., Ljungberg, O., Ringberg, A., Östberg, G., Fernö, M.: Histologic grading in breast cancer: reproducibility between seven pathologic departments. *Acta Oncologica* **39**(1), 41–45 (2000)
- [8] Bonert, M., Tate, A.J.: Mitotic counts in breast cancer should be standardized with a uniform sample area. *BioMedical Engineering OnLine* pp. 1–8 (2017)
- [9] Cireşan, D.C., Giusti, A., Gambardella, L.M., Schmidhuber, J.: Mitosis detection in breast cancer histology images with deep neural networks. *International Conference on Medical Image Computing and Computer-Assisted Intervention* **16**(Pt 2), 411–418 (2013)
- [10] Edmondson, E.F., Hess, A.M., Powers, B.E.: Prognostic Significance of Histologic Features in Canine Renal Cell Carcinomas. *Veterinary Pathology* **52**(2), 260–268 (2014)
- [11] Elston, C.W., Ellis, I.O.: pathological prognostic factors in breast cancer. I. The value of histological grade in breast cancer: experience from a large study with long-term follow-up. *Histopathology* **19**(5), 403–410 (1991)
- [12] Fauzi, M.F.A., Pennell, M., Sahiner, B., Chen, W., Shana’ah, A., Hemminger, J., Gru, A., Kurt, H., Losos, M., Joehlin-Price, A., Kavran, C., Smith, S.M., Nowacki, N., Mansor, S., Lozanski, G., Gurcan, M.N.: Classification of follicular lymphoma: the effect of computer aid on pathologists grading. *BMC Medical Informatics and Decision Making* **15**(1), 115 (2015)
- [13] He, K., Zhang, X., Ren, S., Sun, J.: Deep Residual Learning for Image Recognition. In: *2016 IEEE Conference on Computer Vision and Pattern Recognition (CVPR)*, pp. 770–778. IEEE (2016)
- [14] Kingma, D.P., Ba, J.L.: Adam: A method for stochastic optimization. In: *Proc. 3rd Int. Conf. Learn. Representations* (2015)
- [15] Kirpensteijn, J., Kik, M., Rutteman, G.R., Teske, E.: Prognostic Significance of a New Histologic Grading System for Canine Osteosarcoma. *Veterinary Pathology* **39**(2), 240–246 (2002)
- [16] Kiupel, M., Webster, J.D., Bailey, K.L., Best, S., DeLay, J., Detrisac, C.J., Fitzgerald, S.D., Gamble, D., Ginn, P.E., Goldschmidt, M.H., Hendrick, M.J., Howerth, E.W., Janovitz, E.B., Langohr, I., Lenz, S.D., Lipscomb, T.P., Miller, M.A., Misdorp, W., Moroff, S., Mullaney, T.P., Neyens, I., O’Toole, D., Ramos-Vara, J., Scase, T.J., Schulman, F.Y., Sledge, D., Smedley, R.C., Smith, K., W Snyder, P., Southorn, E., Stedman, N.L., Steficek, B.A., Stromberg, P.C., Valli, V.E., Weisbrode, S.E., Yager, J., Heller, J., Miller, R.: Proposal of a 2-Tier Histologic Grading System for Canine Cutaneous Mast Cell Tumors to More Accurately Predict Biological Behavior. *Veterinary Pathology* **48**(1), 147–155 (2011)

- [17] Li, C., Wang, X., Liu, W., Latecki, L.J.: DeepMitosis: Mitosis detection via deep detection, verification and segmentation networks. *Medical Image Analysis* **45**, 121–133 (2018)
- [18] Loukopoulos, P., Robinson, W.F.: Clinicopathological Relevance of Tumour Grading in Canine Osteosarcoma. *Journal of Comparative Pathology* **136**(1), 65–73 (2007)
- [19] Lozanski, G., Pennell, M., ah, A.S., Zhao, W., Gewirtz, A., Racke, F., Hsi, E., Simpson, S., Mosse, C., Alam, S., Swierczynski, S., Hasserjian, R., Gurcan, M.: Inter-reader variability in follicular lymphoma grading: Conventional and digital reading. *Journal of pathology informatics* **4**(1), 30 (2013)
- [20] Malon, C., Brachtel, E., Cosatto, E., Graf, H.P., Kurata, A., Kuroda, M., Meyer, J.S., Saito, A., Wu, S., Yagi, Y.: Mitotic Figure Recognition: Agreement among Pathologists and Computerized Detector. *Analytical Cellular Pathology* **35**(2), 97–100 (2012)
- [21] Martin, A.R., Weisenburger, D.D., Chan, W.C., Ruby, E.I., Anderson, J.R., Vose, J.M., Bierman, P.J., Bast, M.A., Daley, D.T., Armitage, J.O.: Prognostic value of cellular proliferation and histologic grade in follicular lymphoma. *Blood* **85**(12), 3671–3678 (1995)
- [22] Meuten, D., Munday, J.S., Hauck, M.: Time to Standardize? Time to Validate? *Veterinary Pathology* **55**(2), 195–199 (2018)
- [23] Meuten, D.J.: Appendix: Diagnostic Schemes and Algorithms. In: *Tumors in Domestic Animals*, pp. 942–978. John Wiley & Sons, Inc., Hoboken, NJ, USA (2016)
- [24] Meuten, D.J., Moore, F.M., George, J.W.: Mitotic Count and the Field of View Area. *Veterinary Pathology* **53**(1), 7–9 (2016)
- [25] Meyer, J.S., Alvarez, C., Milikowski, C., Olson, N., Russo, I., Russo, J., Glass, A., Zehnbauser, B.A., Lister, K., Parwaresch, R.: Breast carcinoma malignancy grading by Bloom-Richardson system vs proliferation index: Reproducibility of grade and advantages of proliferation index. *Modern Pathology* **18**(8), 1067–1078 (2005)
- [26] Meyer, J.S., Cosatto, E., Graf, H.P.: Mitotic index of invasive breast carcinoma. Achieving clinically meaningful precision and evaluating tertial cutoffs. *Archives of pathology & laboratory medicine* **133**(11), 1826–1833 (2009)
- [27] Oquab, M., Bottou, L., Laptev, I., Sivic, J.: Is object localization for free? - Weakly-supervised learning with convolutional neural networks. In: *Proceedings of IEEE Conference on Computer Vision and Pattern Recognition*, pp. 685–694. IEEE (2015)
- [28] Otsu, N.: A Threshold Selection Method from Gray-Level Histograms. *IEEE Transactions on Systems, Man, and Cybernetics* **9**(1), 62–66 (1979)



- [29] Paeng, K., Hwang, S., Park, S., Kim, M.: A unified framework for tumor proliferation score prediction in breast histopathology. In: *Deep Learning in Medical Image Analysis and Multimodal Learning for Clinical Decision Support*, pp. 231–239. Springer (2017)
- [30] Rahman, M.A., Wang, Y.: Optimizing Intersection-Over-Union in Deep Neural Networks for Image Segmentation. In: *Advances in Visual Computing*, pp. 234–244. Springer, Cham, Cham (2016)
- [31] Ren, S., He, K., Girshick, R.B., 0001, J.S.: Faster R-CNN - Towards Real-Time Object Detection with Region Proposal Networks. *IEEE transactions on pattern analysis and machine intelligence* **39**(6), 1137–1149 (2017)
- [32] Ronneberger, O., Fischer, P., Brox, T.: U-Net - Convolutional Networks for Biomedical Image Segmentation. In: *International Conference on Medical image computing and computer-assisted intervention*, pp. 234–241. Springer International Publishing, Cham (2015)
- [33] Roux, L., Racoceanu, D., Loménie, N., Kulikova, M., Irshad, H., Klossa, J., Capron, F., Genestie, C., Le Naour, G., Gurcan, M.N.: Mitosis detection in breast cancer histological images An ICPR 2012 contest. *Journal of pathology informatics* **4**, 8 (2013)
- [34] Spangler, W.L., Kass, P.H.: The Histologic and Epidemiologic Bases for Prognostic Considerations in Canine Melanocytic Neoplasia. *Veterinary Pathology* **43**(2), 136–149 (2006)
- [35] Veta, M., van Diest, P.J., Willems, S.M., Wang, H., Madabhushi, A., Cruz-Roa, A., Gonzalez, F., Larsen, A.B.L., Vestergaard, J.S., Dahl, A.B., Cireşan, D.C., Schmidhuber, J., Giusti, A., Gambardella, L.M., Tek, F.B., Walter, T., Wang, C.W., Kondo, S., Matuszewski, B.J., Precioso, F., Snell, V., Kittler, J., de Campos, T.E., Khan, A.M., Rajpoot, N.M., Arkoumani, E., Lacle, M.M., Viergever, M.A., Pluim, J.P.W.: Assessment of algorithms for mitosis detection in breast cancer histopathology images. *Medical Image Analysis* **20**(1), 237–248 (2015)
- [36] Veta, M., Heng, Y.J., Stathonikos, N., Bejnordi, B.E., Beca, F., Wollmann, T., Rohr, K., Shah, M.A., Wang, D., Rousson, M., Hedlund, M., Tellez, D., Ciompi, F., Zerhouni, E., Lanyi, D., Viana, M., Kovalev, V., Liauchuk, V., Phoulady, H.A., Qaiser, T., Graham, S., Rajpoot, N., Sjöblom, E., Molin, J., Paeng, K., Hwang, S., Park, S., Jia, Z., Chang, E.I.C., Xu, Y., Beck, A.H., van Diest, P.J., Pluim, J.P.W.: Predicting breast tumor proliferation from whole-slide images: the tupac16 challenge. *arXiv preprint arXiv:1807.08284* (2018)
- [37] Zhou, B., Khosla, A., Lapedriza, À., Oliva, A., Torralba, A.: Learning Deep Features for Discriminative Localization. In: *2016 IEEE Conference on Computer Vision and Pattern Recognition (CVPR)*, pp. 2921–2929. IEEE (2016)